Astrophysical Journal Letters 906.2 (2021): L6

DOI: https://doi.org/10.3847/2041-8213/abd32f

Draft version December 16, 2020
Typeset using LaTeX twocolumn style in AASTeX63

MUSE reveals extended circumnuclear outflows in the Seyfert 1 NGC 7469

A. C. Robleto-Orús,[1] J. P. Torres-Papaqui,[1] A. L. Longinotti,[2,3] R. A. Ortega-Minakata,[4]
S. F. Sánchez,[3] Y. Ascasibar,[5] E. Bellocchi,[6] L. Galbany,[7] M. Chow-Martínez,[8,1]
J. J. Trejo-Alonso,[9] A. Morales-Vargas,[1] and F. J. Romero-Cruz[1,10]

[1]Departamento de Astronomía, Universidad de Guanajuato, Apdo. 144, C.P. 36000 Guanajuato, Gto., Mexico
[2]Instituto Nacional de Astrofísica, Óptica y Electrónica, C.P. 72840, Tonantzintla, Puebla, Mexico
[3]Instituto de Astronomia, Universidad Nacional Autónoma de México, C.P. 04510, CDMX, Mexico
[4]Instituto de Radioastronomía y Astrofísica, Universidad Nacional Autónoma de México, C.P. 58089, Morelia, Mich., Mexico
[5]Departamento de Física Teórica,Universidad Autónoma de Madrid, C.P. 28049 Madrid, Spain
[6]Centro de Astrobiología (CSIC-INTA), ESAC, Urb. Villafranca del Castillo, E-28691 Villanueva de la Cañada, Madrid, Spain
[7]Departamento de Física Teórica y del Cosmos, Universidad de Granada, C.P. 18071, Granada, Andalucía, Spain
[8]Instituto de Geología y Geofísica IGG-CIGEO, Universidad Nacional Autónoma de Nicaragua, C.P. 663, Managua, Nicaragua
[9]Facultad de Ingeniería, Universidad Autónoma de Querétaro, C.P. 76010, Santiago de Querétaro, Qro., Mexico
[10]Instituto Tecnológico Superior de Guanajuato. C. P. 36262, Guanajuato, Gto. Mexico

ABSTRACT

NGC 7469 is a well-known Luminous IR Galaxy, with a circumnuclear star formation ring ($\sim$ 830 pc radius) surrounding a Seyfert 1 AGN. Nuclear unresolved winds were previously detected in X-rays and UV, as well as an extended biconical outflow in IR coronal lines. We search for extended outflows by measuring the kinematics of the Hβ and [O III] λ5007 optical emission lines, in data of the VLT/MUSE integral field spectrograph. We find evidence of two outflow kinematic regimes: one slower regime extending across most of the star formation ring—possibly driven by the massive star formation—and a faster regime (with a maximum velocity of -715 km s^{-1}), only observed in [O III], in the western region between the AGN and the massive star forming regions of the ring, likely AGN-driven. This work shows a case where combined AGN/star-formation feedback can be effectively spatially-resolved, opening up a promising path toward a deeper understanding of feedback processes in the central kiloparsec of AGN.

Keywords: Active galactic nuclei — Galaxy winds

1. INTRODUCTION

Studies over large samples of galaxies have revealed ionized gas outflows associated both with star formation (SF) (e.g. Ho et al. 2014; Roche et al. 2015; López-Cobá et al. 2017a, 2019) and with active galactic nuclei (AGN) (e.g. Greene & Ho 2005; Woo et al. 2016; Perna et al. 2017; Wylezalek et al. 2020), significantly improving our understanding of the role of AGN and SF in feedback processes.

Optical emission lines can trace the warm-ionized phase ($T \sim 10^3$–10^4 K) of outflows, reaching line-of-sight velocities ($LoSVs$) of 10^2–10^3 km s^{-1}, and spatial scales up to $\sim 10^3$ pc (Cicone et al. 2018, and references therein). The collisionally-excited [O III]λ5007 emission line—weakly affected by blending with nearby lines, and usually presenting high signal-to-noise ratio (S/N) in AGN—is a popular tracer of outflows, used to study possible connections with winds in other spectral bands (e.g., Mullaney et al. 2013; Perna et al. 2017; Venturi et al. 2018).

Woo et al. (2016) studied outflow kinematics with [O III]λ5007 and Hα for a large sample of type 2 AGN at $z \leq 0.3$, finding that higher outflow velocities correspond to higher velocity dispersions and luminosities. The gas velocity and velocity dispersion were more extreme for [O III]λ5007 than for Hα, suggesting that Hα traces the nebular emission from SF regions—with their motion dominated by the host galaxy gravitational potential—and that [O III]λ5007 traces mainly the AGN-driven outflow.

Corresponding author: A. C. Robleto-Orús
ac.robletoorus@ugto.mx

Consistent results were reported by Karouzos et al. (2016) studying the spatially resolved kinematics of outflows in six type 2 AGN ($z \sim 0.05$–0.1), using integral-field-spectroscopy (IFS) with GMOS/Gemini. They confirmed that Hα follows the kinematics of stellar absorption lines, while [O III]λ5007 has independent and more extreme kinematics. High spatial and spectral resolution IFS has boosted knowledge of geometry and physics of galaxy-scale AGN-driven outflows in nearby galaxies (i.e., López-Cobá et al. 2017b; Mingozzi et al. 2019; López-Cobá et al. 2020).

1.1. *NGC 7469: starburst and AGN*

NGC 7469 is a nearby galaxy hosting a Seyfert type 1 AGN with a supermassive black hole mass $\log_{10} M_{BH} = 7.32^{+0.09}_{-0.10}$ M and bolometric luminosity $L_{bol} =\sim 10^{45}$ erg s^{-1} (Ponti et al. 2012). It is classified as a luminous infrared galaxy (LIRG) due to the starburst concentrated in its circumnuclear ring, triggered by interaction with the IC 5283 galaxy. The ring outer radius is 2.5″ ($\sim$ 830 pc) and the inner radius 0.7" ($\sim$ 232 pc), with bright knots at $\sim$ 1.5″ ($\sim$ 500 pc) (Genzel et al. 1995). This ring contains young (1–20 Myr) massive stars (Diaz-Santos et al. 2007).

Davies et al. (2004) and Izumi et al. (2015) found molecular gas structures in the central region using millimeter observations, including a circumnuclear disk ($\sim$ 300 pc) that Izumi et al. (2020) revealed to be an X-ray dominated region produced by the AGN.

Blustin et al. (2007) reported X-ray spatially-unresolved nuclear winds (warm absorbers) with LoSVs of -580 to -2300 km s^{-1}, later confirmed by Behar et al. (2017) and Mehdipour et al. (2018) at $LoSVs$ of -400 to -1800 km s^{-1} within a distance of 2–80 pc from the black hole. All these authors reported UV counterparts of the X-ray winds.

Müller-Sánchez et al. (2011) found a biconical outflow in the infrared coronal line [Si VI]$\lambda 1.96\mu$m using VLT/SINFONI and Keck/Osiris IFS, extending up to 380 $\pm$ 25 pc from the AGN, with a maximum velocity of $\sim$ 130 km s^{-1} at 220 $\pm$ 25 pc.

While this outflow was not reported in recent optical IFS observations with GTC/MEGARA by Cazzoli et al. (2020), they described a non-rotational turbulent component that might be associated with it.

We report, for the first time, optical extended ionized outflows in the circumnuclear region of NGC 7469, based on the kinematics of the [O III]λ5007 and Hβ emission lines. The comoving distance to NGC 7469 is 69.64 Mpc[1] ($z = 0.01632$, Keel 1996), adopting a standard ΛCDM cosmology ($H_0 = 70$ km s^{-1} Mpc^{-1}, $\Omega_\Lambda = 0.7$ and $\Omega_M = 0.3$).

2. METHODOLOGY

2.1. *Observations and data reduction*

NGC 7469 was observed in 2014 August 19, during the science verification run of the Multi Unit Spectroscopic Explorer (MUSE, Bacon et al. 2004) IFS instrument at the Very Large Telescope (VLT) of the European Southern Observatory (ESO, Chile). The pilot study of the All-weather MUse Supernova Integral-field of Nearby Galaxies survey (AMUSING, Galbany et al. 2016) and the AMUSING++ compilation[2] (López-Cobá et al. 2020) include these data. MUSE covers a field of view of 1 arcmin^2 with a spatial sampling of 0.2″ per spaxel (top-left panel, figure 1). For NGC 7469 each spaxel presents a scale of 66.44 pc (332.2 pc arcsec^{-1}). The seeing had a $FWHM = 1.23''$ ($\sim$ 409 pc). Data reduction followed the standard procedures, using the REFLEX (Freudling et al. 2013) package and the MUSE pipeline (Weilbacher et al. 2014). We corrected for systemic velocity using the value by Keel (1996) (4898 $\pm$ 5 km s^{-1}), obtained by a combination of emission-line methods due to the absence of absorption lines in the central region.

2.2. *AGN/host galaxy deblending*

Beam-smearing—the scattering of light from the spatially unresolved broad-line region (BLR) and inner narrow-line region (NLR) due to seeing—can lead to overestimation of the size of the extended narrow-line region (ENLR) and of the velocity of associated outflows in type 1 AGN (Husemann et al. 2016). This effect was corrected through the QDEBLEND3D software described in Husemann et al. (2012, 2014, 2016). We assume a surface brightness model for the host galaxy, fixing brightness, effective radius, Sersic index and axis ratio, with values from Bentz et al. (2009). QDEBLEND3D produces two data cubes (figure 1): one contains the AGN continuum and emission from the BLR and the NLR (hereafter "AGN data cube"); the other contains the host galaxy stellar continuum, SF regions and the ENLR (hereafter "Host data cube").

2.3. *Continuum subtraction*

We subtract a synthetic stellar continuum template from each spectrum in the Host data cube, to obtain

[1] Using the Ned Wright Cosmology Calculator (Wright 2006).

[2] http://ifs.astroscu.unam.mx/AMUSING++/index.php?start=24

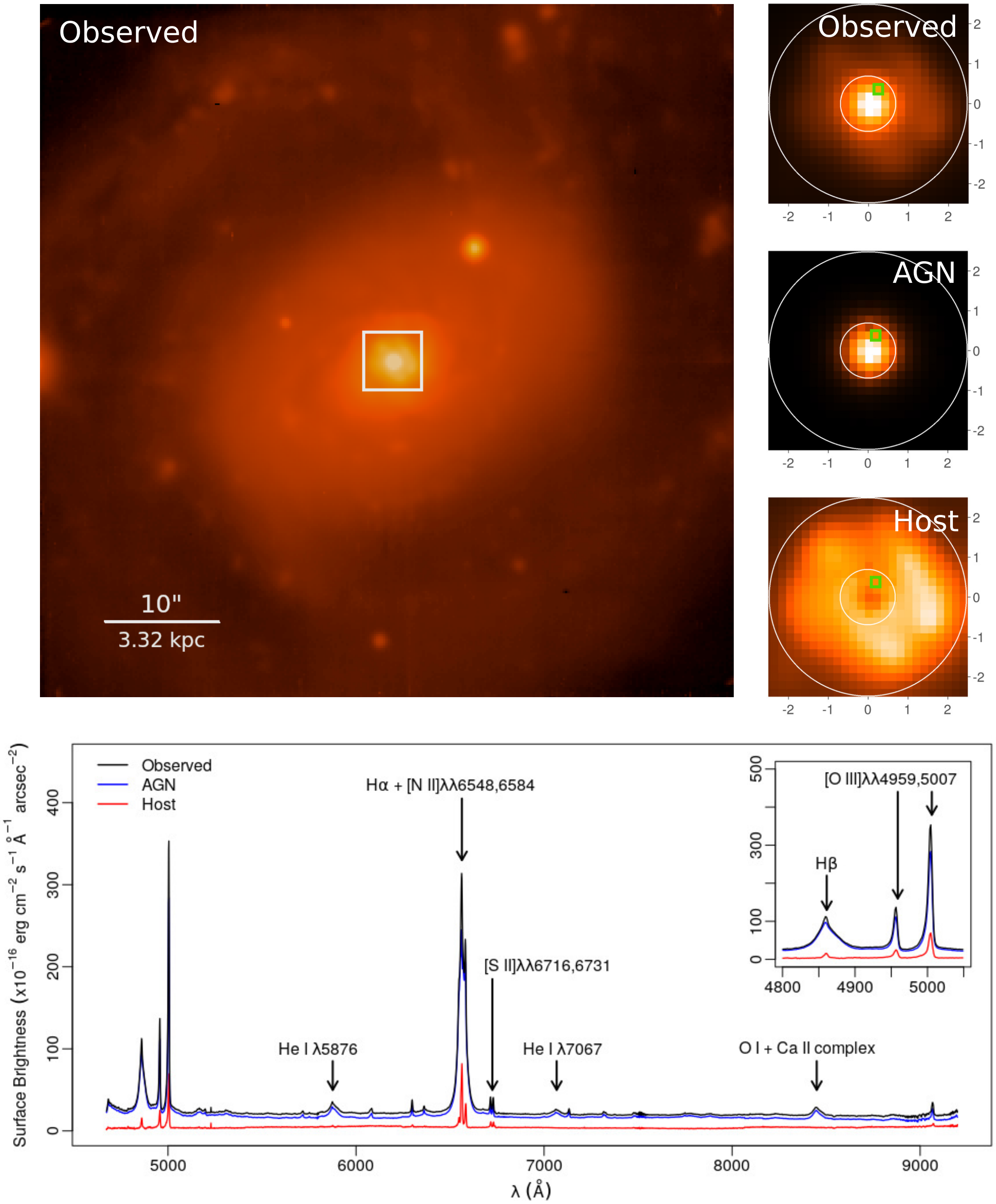

Figure 1. Top-left: MUSE "white" image (all wavelengths integrated) of NGC7469. The white square encloses the 5″ × 5″ field explored in this study. North is up and east is left. Right: a zoom into the 5″ × 5″ field for the Observed, AGN and Host data cubes resulting of the deblending process. The white circles are the inner and outer limits of the SF ring, as proposed by Genzel et al. (1995). Axes units are in arcseconds. Bottom: spectrum extracted from the spaxel marked in green in the right-side panels, showing the deblended spectra. Since this spaxel is close to the center (∼ 0.4″), the AGN dominates the flux of the spectrum.

"pure-emission" spectra. We create the templates (after correcting for Galactic extinction using dust maps produced by Schlegel et al. 1998) using the STARLIGHT population synthesis code (Cid Fernandes et al. 2005).

We use the base set of 150 simple stellar populations[3] selected by Asari et al. (2007)—25 ages (1×10^6–1.8×10^{10} yr) and 6 metallicities (0.005–2.5 Z)—with the Chabrier (2003) initial mass function. Emission lines are masked out. Intrinsic extinction is corrected in the process using the Cardelli et al. (1989) reddening law ($R_V = 3.1$).

We study the line profiles of [O III]$\lambda\lambda$4959, 5007 and Hβ in a box 5″ (1.611 kpc) wide, centerd on the AGN, that contains the SF ring and corresponds to the field studied by Diaz-Santos et al. (2007) (figure 1). The line profiles of many spaxels are asymmetric and broadened at their bases, suggesting the presence of winds. We characterize these features using two approaches (see below).

The results of [O III]λ4959 and [O III]λ5007 are consistent, including the expected one-third flux ratio. We only report here the results for [O III]λ5007 (hereafter [O III]), due to its higher S/N.

2.4. *Non-parametric approach*

Following Harrison et al. (2014), each emission line is fitted with three Gaussian components (figure 2a), whose sum creates a synthetic line profile. To fit the Gaussians we use the Levenberg-Marquardt algorithm (Marquardt 1963), implemented with the IDL MPFIT libraries (Markwardt 2009). Spectra were interpolated, resulting in $\approx$ 50 data points per emission line, versus $\approx$ 10 in the original data. This increases the chance of obtaining a good solution by decreasing the solution space, and reduces computing time. We reject all Gaussian components with $S/N < 3$.

We avoid physically interpreting the Gaussians. Instead we characterize the kinematics by deriving quantities from the cumulative function of the whole synthetic line profile: the offset velocity Δv (the mean of the velocities at the 5th and 95th percentiles) the width at 80% of the flux W_{80}, and the $FWHM$. Hence Δv measures the asymmetry of the line profile related with gas motion on the line of sight; the sign indicates the direction. The $W_{80}/FWHM$ ratio is the relative broadening at the base of the line.

López-Cobá et al. (2020) uses an alternative non-parametric approach, however the current approach is accurate enough for our goal.

2.5. *Two-Gaussian components approach*

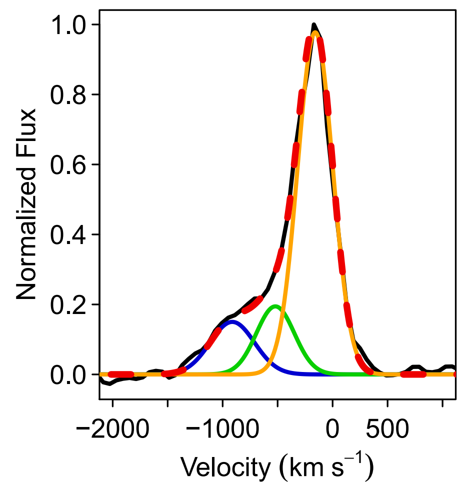

(a)

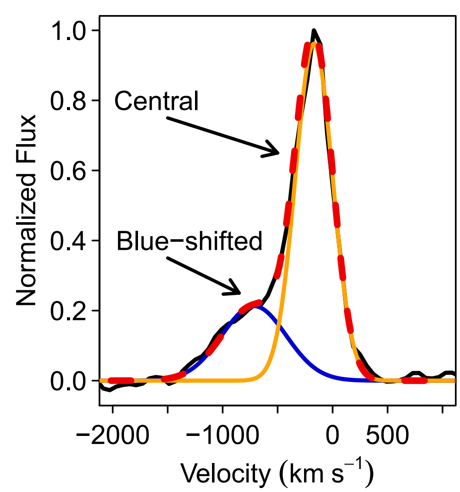

(b)

Figure 2. Examples of (a) three-Gaussian fit and (b) two-Gaussian fit of [O III]λ5007. The solid black line represents the Host data cube spectrum after subtracting the stellar continuum. The red-dashed line is the synthetic line profile resulting from the sum of the components.

We fit two Gaussian components to the [O III] line (figure 2b) following the approach by Woo et al. (2016) and Karouzos et al. (2016). The Gaussian component closest to the rest-frame velocity (hereafter, *central component*), is related with gas dominated by the host galaxy gravitational potential, rotating in the galactic disk; the second Gaussian component accounts for the outflowing gas as a whole (hereafter, *blueshifted component*). See figure 2b.

We apply the same fitting method described in section 2.4. We measure the kinematic parameters of each

[3] We use the 2016 version of the MILES libraries, an update of ones by Bruzual & Charlot 2003: http://www.bruzual.org/bc03/Updated_version_2016/

Gaussian component: the line-of-sight velocity ($LoSV$) from the Doppler shift of the Gaussian peak with respect to the rest frame, and the velocity dispersion (σ) from the $FWHM$—corrected for the instrumental width ($FWHM_{inst} \sim 158$ km s^{-1} for [O III]).

2.6. *Uncertainties*

We estimate uncertainties through Monte Carlo simulations, following Lenz & Ayres (1992), iterating 1000 times. For the non-parametric approach, the mean uncertainties across the studied field are: ~ 3.9, ~ 6.7 and ~ 6.6 km s^{-1} for Δv, W_{80} and the $FWHM$ of [O III], respectively. For Hβ the corresponding values are ~ 2.9, ~ 6.5 and ~ 6.6 km s^{-1}.

For the two Gaussian components approach, the mean uncertainties in $LoSV$ and σ are, respectively, ~ 60 and ~ 32 km s^{-1} for the [O III] blueshifted component and ~ 30 and ~ 6.6 km s^{-1} for the central component.

3. RESULTS

3.1. *Non-parametric approach*

Figure 3 shows the maps of Δv, W_{80} and $W_{80}/FWHM$ for [O III] and Hβ. As a reference for the position of the AGN and the massive SF regions of the ring, the maps are overlapped to the Hubble Space Telescope (HST) ACS F330W near-UV image[4]. Projections of the edges of the [Si VI]$\lambda 1.96\mu$m outflow by Müller-Sánchez et al. (2011) are shown, with the blueshifted cone pointing west and the red-shifted cone pointing east.

The [O III] results reveal the existence of two outflow kinematic regimes, located in different regions. In figure 3a, in a region labelled as "A", a strong [O III] blueshifted asymmetry (Δv up to -310 km s^{-1}, reaching ~ 531 pc ($\sim 1.6''$) to the north) extends northwest of the center, in between the AGN and the massive SF regions of the ring. Approximately half of it extends within the limits of the projected west [Si VI]$\lambda 1.96\mu$m cone, while the rest lies outside to the north.

This region also presents a broadening of $W_{80} > 600$ km s^{-1} and $W_{80}/FWHM > 3$ (figures 3b and 3c). This high asymmetry and broadening are strong kinematic evidence of the presence of an outflow in the "A" region.

The existence of a second kinematic regime in the rest of the ring and the inner regions is disclosed by less prominent asymmetry ($-200 \leq \Delta v \leq -100$ km s^{-1}) and broadening ($250 < W_{80} < 500$ km s^{-1} and $1.5 < W_{80}/FWHM < 3$). We ignore here the outer regions of the field due to their lower S/N.

The Hβ maps show only one outflow regime, similar to the slowest one observed in [O III]. The Δv, W_{80} and $W_{80}/FWHM$ maps are shown in figures 3d, 3e and 3f, respectively. Outside the "A" region, Hβ has similar but less pronounced Δv than [O III], with most spaxels having $\Delta v > -200$ km s^{-1}.

Low $W_{80}/FWHM < 2$ ratios dominate the field except for the western SF ring. Despite reaching $W_{80} > 300$ km s^{-1} (with a maximum of ~ 640 km s^{-1}), they keep $W_{80}/FWHM < 3$. High $FWHM$ values keep low $W_{80}/FWHM$ ratios, possibly due to the presence of turbulence or shocks, not only in the wind but also in the bulk of the gas, affecting the whole line profiles.

3.2. *Two-Gaussians approach*

Figure 4a shows the $LoSV$ map of the [O III] blueshifted component. The two outflow regimes found in Section 3.1 are confirmed, with different $LoSV$ ranges of the blueshifted component: high velocities ($LoSV < -400$ km s^{-1}) are found in the "A" region; lower velocities ($LoSV > -400$ km s^{-1}) are found around the rest of the field. The high $LoSV$ spaxels in figure 4a, cover a smaller area than that of the high Δv spaxels in figure 3a. The fastest blueshifted component (shown at figure 2b) reaches $LoSV = -715$ km s^{-1}, at ~ 240 pc ($\sim 0.7''$) northwest of the center. Velocity dispersion values of σ (> 300 km s^{-1}) do appear in the the "A" region (figure 4b), similar to W_{80}, but they extend further over the western massive SF regions.

The velocity–velocity dispersion (VVD) diagram (Woo et al. 2016; Karouzos et al. 2016) provides a straightforward visualization of the different kinematic regimes (figure 4c). Once the central and blueshifted components are plotted in the VVD, the former is clearly is separated from the latter in the parameter space. Following Woo et al. (2016) and Karouzos et al. (2016) interpretation, the more extreme kinematics of the blueshifted component could be evidence of outflows (not dominated by the gravitational potential of the host galaxy), while the positive and negative $LoSV$ values of the central component suggest motion in a galactic disk.

The high $LoSV$ spaxels in the "A" region of figure 4a (with a median $LoSV$ of -581 km s^{-1} and median σ of 300 km s^{-1}) are clearly separated from the bulk of the blueshifted components (with median $LoSV$ and σ of -284 and 188 km s^{-1}, respectively) consistent with the existence of the two kinematic regimes in the blueshifted component.

Note that if the mean $LoSV$ of the central component was assumed as systemic reference frame, the outflow

[4] HSTScI public archive through the MAST web tool.

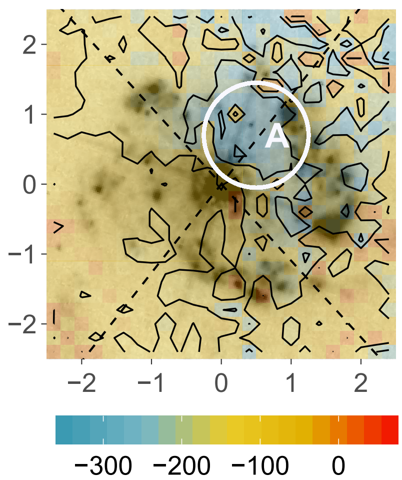

(a) [O III] Δv (km s^{-1})

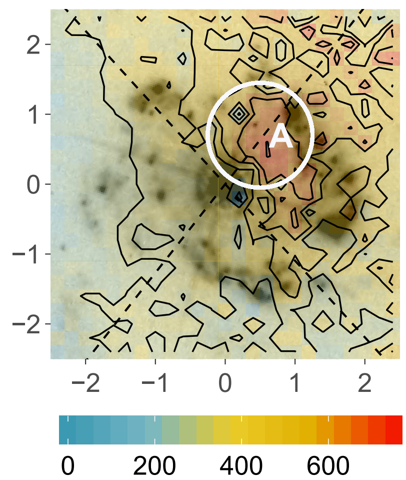

(b) [O III] W_{80} (km s^{-1})

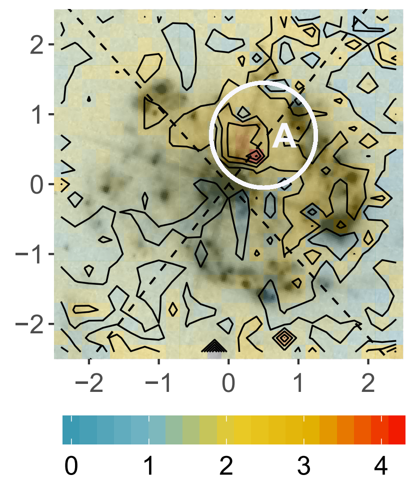

(c) [O III] $W_{80}/FWHM$

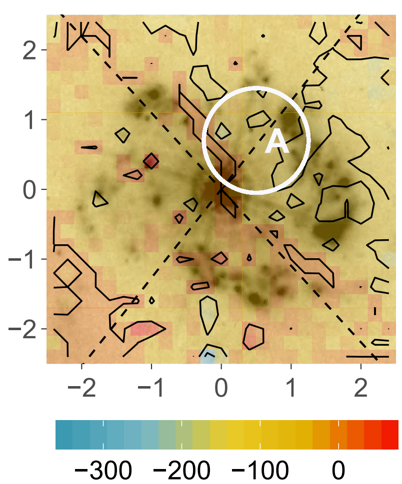

(d) Hβ Δv (km s^{-1})

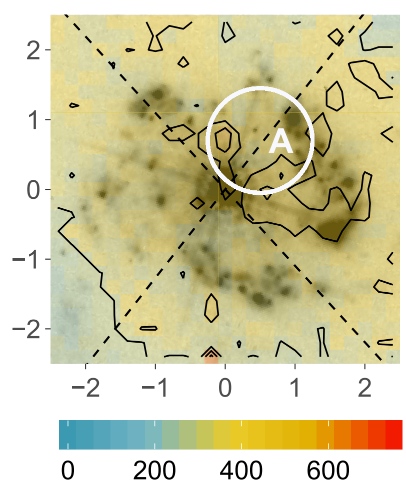

(e) Hβ W_{80} (km s^{-1})

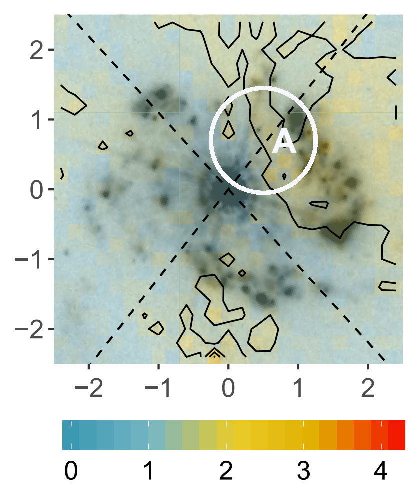

(f) Hβ $W_{80}/FWHM$

Figure 3. Maps from the non-parametric approach for [O III] (a, b and c) and Hβ (d, e and f), superimposed over the HST/ACS F330W image. North is up and east is left, axes units are in arcseconds. The AGN is located at the center. The diagonal dashed lines represent the projection on the plane of the sky of the biconical [Si VI]$\lambda 1.96\mu$m outflow, with the blue side pointing west and the red side pointing east. The approximate position of the fast [O III] outflow is marked with a white "A" and a circle (radius and position are merely orientative).

velocity would be 134 km s^{-1} slower. However, the existence of both outflow regimes would still hold solidly, with the slower gas mean $LoSV \sim -150$km s^{-1}. In fact, more than one Gaussian is needed to fit the line profiles, as shown by the non-parametric approach.

3.3. *BPT diagnostics of the central component*

The BPT diagnostic diagram (Baldwin et al. 1981) informs on the excitation mechanisms, provided that only Gaussian components with similar kinematics, i.e. tracing the same bulk of gas, are considered. The blueshifted component kinematics of [O III] and Hβ are inconsistent for many spaxels, and shall not be combined in the same diagram. Due to blending of the shifted components, we could unambiguously identify only the peaks of the central components in the Hα-[N II] complex and use them for BPT diagnostics.

Figure 5 shows the BPT-NII diagnostics—based on the [O III]λ5007/Hβ and [N II]λ6584/Hα line ratios—of the central component. The mean flux uncertainties

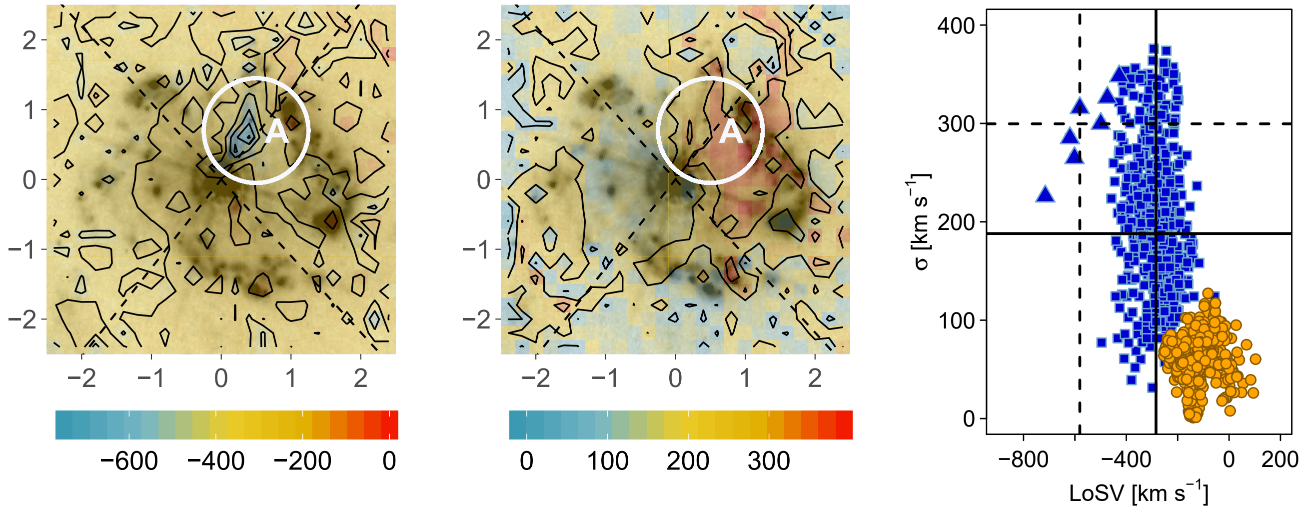

(a) [O III] blueshifted component *LoSV* (km s^{-1})

(b) [O III] blueshifted component σ (km s^{-1})

(c) [O III] VVD diagram

Figure 4. Maps of (a) *LoSV* and (b) σ for the blueshifted component of [O III]. Description is the same as in figure 3. (c) VVD diagram for [O III]. The symbols correspond to the central component (orange circles), blueshifted component (blue squares) and the high-velocity blueshifted component ($LoSV < -400$ km s^{-1}) spaxels in the "A" region (blue triangles). The dashed lines are the median values for the high-velocity spaxels while the solid lines are the median values for the rest of the blueshifted components. The central component has a mean $LoSV = -134$ km s^{-1}. Should this value be assumed as the systemic rest frame, the existence of both outflow regimes would still hold since at least two Gaussians are necessary to fit the line profiles.

(in $\times 10^{-17}$ erg cm^{-2} s^{-1} units) are $\sim$ 0.58 for [O III], $\sim$ 0.52 for Hβ, $\sim$ 0.76 for [N II]λ6584 and $\sim$ 3.4 for Hα.

AGN excitation dominates the northeast quadrant up to $\sim$ 500 pc from the center, while a combination of SF and transition-object-like (TO) excitation extends across the rest of the field (LINER-like excitation is scarce). The "A" region with the fastest [O III] outflow presents a combination of AGN, TO and SF excitation, the latter over the massive SF regions of the ring. We use this result as exploratory; direct extension to the blueshifted component should be avoided. More detailed analysis will be presented in a future paper.

4. DISCUSSION

Both kinematic analyses indicate two [O III] outflow regimes: the "A" region shows more extreme [O III] outflow kinematics compared to the rest of the field (figures 3a, 3b, 3c, 4a, 4b); this is reflected in the VVD diagram (figure 4c).

Hβ and [O III] winds behave similarly across the field, except for the "A" region, where the behaviour of [O III] is more extreme. The Hβ maps (figures 3d, 3e and 3f) show a slight increment in Δv and $W_{80}/FWHM$ in the "A" region, but not as pronounced as with [O III].

Based purely on kinematic criteria, a stellar origin for the slow Hβ and [O III] outflows would be consistent with them extending across most of the SF ring. The AGN is probably driving the faster [O III] outflow regime: it presents more extreme kinematics, with similar *LoSV*s to those AGN-driven outflows reported by Woo et al. (2016) and Karouzos et al. (2016) in [O III] (projection effects on the *LoSV* should be considered).

The high-σ values of the [O III] blueshifted component and the low Hβ $W_{80}/FWHM$ ratios (but high W_{80} values) at the "A" region suggest the presence of shocks both in the wind and in the gravitationally-bounded gas. Therefore, interaction between the AGN-driven and SF-driven winds in this region is a possibility.

As for the excitation mechanisms, the BPT-NII map of the central component (gas in the galactic disk) in figure 5b shows that emission in most of region "A" and the north-east quadrant is consistent with a combination of AGN and SF excitation, while the rest of the field is consistent with SF excitation (although AGN contribution cannot be excluded).

The fast [O III] outflow partially overlaps with the blueshift cone of the AGN-driven outflow traced by [Si VI]λ1.96μm. If both oxygen and silicon were photoionized by the AGN, the geometry of the AGN radiation field could determine the spatial distribution of their emission, with [Si VI]λ1.96μm being detected where the density of high-energy photons was higher—Si^{+5} has a higher ionization potential than O^{++} (167 versus 35.1 eV).

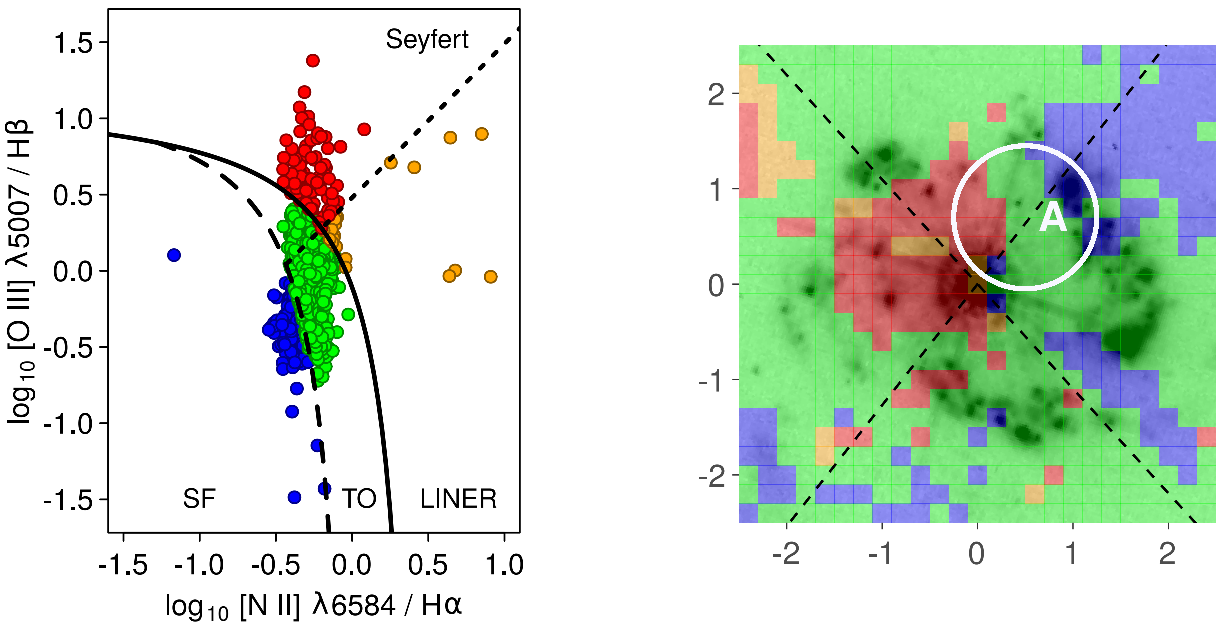

(a) (b)

Figure 5. (a) BPT-NII diagram of the central component, used to determine the main excitation mechanism in each spaxel: star formation (SF), transition object (TO), low ionization nuclear emission line region (LINER) and Seyfert. The dividing lines correspond to Kewley et al. (2001) (solid), Kauffmann et al. (2003) (dashed) and Fernandes et al. (2010) (dotted). (b) BPT-NII map, the color of each spaxel corresponds to its position in the diagnostic diagram. Other elements are the same as in figure 3.

All this makes plausible the following scenario: the slow outflow could be driven by SF regions while the fast outflow could be driven by the AGN. However, evidence is not conclusive. BPT diagnostics of the blueshifted component will test our proposed scenario by providing insights on the excitation mechanisms in the outflowing gas. We are working on that analysis; results will be presented in a future paper.

The beam-smearing correction here applied for the first time to NGC 7469 (e.g. Cazzoli et al. 2020; López-Cobá et al. 2020), proved to be crucial to remove the AGN spectral contribution, allowing detection of the outflows.

Confirmation that these outflows were driven by the SF and the AGN, would make of NGC 7469—a galaxy close enough to spatially distinguish their sources—an outstanding case for studying combined feedback effects.

ACKNOWLEDGEMENTS

We thank the referee for the careful review of our paper and insightful comments that have improved the quality of our work. Support from CONACyT (Mexico) grant CB-2016-01-286316 is acknowledged. We are thankful to Bernd Husemann for helping with QDeblend3D installation. ACRO thanks Vital Fernández for advice and discussions. JPTP acknowledges DAIP-UGto (Mexico) for granted support (0173/2019). YA aknowledges support from project PID2019-107408GB-C42 (Ministerio de Ciencia e Innovación, Spain). SFS thanks the support of CONACYT grants CB-285080 and FC-2016-01-1916, and funding from the PAPIIT-DGAPA-IN100519 (UNAM) project. LG was funded by the European Union's Horizon 2020 research and innovation programme under the Marie Skłodowska-Curie grant agreement No.839090. This work has been partially supported by the Spanish grant PGC2018-095317-B-C21 within the European Funds for Regional Development (FEDER).

Software: **REFLEX (Freudling et al. 2013), MUSE pipeline (Weilbacher et al. 2014), Starlight (Cid Fernandes et al. 2005), QDeblend3D (Husemann et al. 2012), MPFIT (Markwardt 2009)**

REFERENCES

Asari, N. V., Cid Fernandes, R., Stasińska, G., et al. 2007, MNRAS, 381, 263, doi: 10.1111/j.1365-2966.2007.12255.x

Bacon, R., Bauer, S.-M., Bower, R., et al. 2004, in Proc. SPIE, Vol. 5492, Ground-based Instrumentation for Astronomy, ed. A. F. M. Moorwood & M. Iye, 1145–1149, doi: 10.1117/12.549009

Baldwin, J. A., Phillips, M. M., & Terlevich, R. 1981, Publications of the Astronomical Society of the Pacific, 93, 5

Behar, E., Peretz, U., Kriss, G. A., et al. 2017, A&A, 601, A17, doi: 10.1051/0004-6361/201629943

Bentz, M. C., Peterson, B. M., Netzer, H., Pogge, R. W., & Vestergaard, M. 2009, ApJ, 697, 160, doi: 10.1088/0004-637X/697/1/160

Blustin, A. J., Kriss, G. A., Holczer, T., et al. 2007, A&A, 466, 107, doi: 10.1051/0004-6361:20066883

Bruzual, G., & Charlot, S. 2003, MNRAS, 344, 1000, doi: 10.1046/j.1365-8711.2003.06897.x

Cardelli, J. A., Clayton, G. C., & Mathis, J. S. 1989, ApJ, 345, 245, doi: 10.1086/167900

Cazzoli, S., Gil de Paz, A., Márquez, I., et al. 2020, Monthly Notices of the Royal Astronomical Society, 493, 3656

Chabrier, G. 2003, PASP, 115, 763, doi: 10.1086/376392

Cicone, C., Brusa, M., Ramos Almeida, C., et al. 2018, Nature Astronomy, 2, 176, doi: 10.1038/s41550-018-0406-3

Cid Fernandes, R., Mateus, A., Sodré, L., Stasińska, G., & Gomes, J. M. 2005, MNRAS, 358, 363, doi: 10.1111/j.1365-2966.2005.08752.x

Davies, R. I., Tacconi, L. J., & Genzel, R. 2004, ApJ, 602, 148, doi: 10.1086/380995

Diaz-Santos, T., Alonso-Herrero, A., Colina, L., Ryder, S. D., & Knapen, J. H. 2007, ApJ, 661, 149, doi: 10.1086/513089

Fernandes, R. C., Stasińska, G., Schlickmann, M., et al. 2010, Monthly Notices of the Royal Astronomical Society, 403, 1036

Freudling, W., Romaniello, M., Bramich, D. M., et al. 2013, A&A, 559, A96, doi: 10.1051/0004-6361/201322494

Galbany, L., Anderson, J. P., Rosales-Ortega, F. F., et al. 2016, MNRAS, 455, 4087

Genzel, R., Weitzel, L., Tacconi-Garman, L. E., et al. 1995, ApJ, 444, 129, doi: 10.1086/175588

Greene, J. E., & Ho, L. C. 2005, ApJ, 627, 721, doi: 10.1086/430590

Harrison, C., Alexander, D., Mullaney, J., & Swinbank, A. 2014, Monthly Notices of the Royal Astronomical Society, 441, 3306

Ho, I.-T., Kewley, L. J., Dopita, M. A., et al. 2014, Monthly Notices of the Royal Astronomical Society, 444, 3894

Husemann, B., Jahnke, K., Sánchez, S. F., et al. 2014, MNRAS, 443, 755, doi: 10.1093/mnras/stu1167

Husemann, B., Scharwächter, J., Bennert, V. N., et al. 2016, A&A, 594, A44, doi: 10.1051/0004-6361/201527992

Husemann, B., Wisotzki, L., Sánchez, S. F., & Jahnke, K. 2012, A&A, 549, A43, doi: 10.1051/0004-6361/201220076

Izumi, T., Kohno, K., Aalto, S., et al. 2015, ApJ, 811, 39, doi: 10.1088/0004-637X/811/1/39

Izumi, T., Nguyen, D. D., Imanishi, M., et al. 2020, arXiv e-prints, arXiv:2006.09406. https://arxiv.org/abs/2006.09406

Karouzos, M., Woo, J.-H., & Bae, H.-J. 2016, The Astrophysical Journal, 819, 148

Kauffmann, G., Heckman, T. M., Tremonti, C., et al. 2003, Monthly Notices of the Royal Astronomical Society, 346, 1055

Keel, W. C. 1996, ApJS, 106, 27, doi: 10.1086/192326

Kewley, L. J., Dopita, M., Sutherland, R., Heisler, C., & Trevena, J. 2001, The Astrophysical Journal, 556, 121

Lenz, D. D., & Ayres, T. R. 1992, PASP, 104, 1104, doi: 10.1086/133096

López-Cobá, C., Sánchez, S. F., Bland-Hawthorn, J., et al. 2019, MNRAS, 482, 4032, doi: 10.1093/mnras/sty2960

López-Cobá, C., Sánchez, S. F., Moiseev, A. V., et al. 2017a, MNRAS, 467, 4951, doi: 10.1093/mnras/stw3355

López-Cobá, C., Sánchez, S. F., Cruz-González, I., et al. 2017b, ApJL, 850, L17, doi: 10.3847/2041-8213/aa98db

López-Cobá, C., Sánchez, S. F., Anderson, J. P., et al. 2020, The Astronomical Journal, 159, 167

Markwardt, C. B. 2009, in Astronomical Society of the Pacific Conference Series, Vol. 411, Astronomical Data Analysis Software and Systems XVIII, ed. D. A. Bohlender, D. Durand, & P. Dowler, 251. https://arxiv.org/abs/0902.2850

Marquardt, D. W. 1963, Journal of the Society for Industrial and Applied Mathematics, 11, 431. http://www.jstor.org/stable/2098941

Mehdipour, M., Kaastra, J. S., Costantini, E., et al. 2018, A&A, 615, A72, doi: 10.1051/0004-6361/201832604

Mingozzi, M., Cresci, G., Venturi, G., et al. 2019, A&A, 622, A146, doi: 10.1051/0004-6361/201834372

Mullaney, J. R., Alexander, D. M., Fine, S., et al. 2013, MNRAS, 433, 622, doi: 10.1093/mnras/stt751

Müller-Sánchez, F., Prieto, M. A., Hicks, E. K. S., et al. 2011, ApJ, 739, 69, doi: 10.1088/0004-637X/739/2/69

Perna, M., Lanzuisi, G., Brusa, M., Mignoli, M., & Cresci, G. 2017, A&A, 603, A99, doi: 10.1051/0004-6361/201630369

Ponti, G., Papadakis, I., Bianchi, S., et al. 2012, A&A, 542, A83, doi: 10.1051/0004-6361/201118326

Roche, N., Humphrey, A., Gomes, J. M., et al. 2015, MNRAS, 453, 2349, doi: 10.1093/mnras/stv1669

Schlegel, D. J., Finkbeiner, D. P., & Davis, M. 1998, The Astrophysical Journal, 500, 525

Venturi, G., Nardini, E., Marconi, A., et al. 2018, A&A, 619, A74, doi: 10.1051/0004-6361/201833668

Weilbacher, P. M., Streicher, O., Urrutia, T., et al. 2014, in Astronomical Society of the Pacific Conference Series, Vol. 485, Astronomical Data Analysis Software and Systems XXIII, ed. N. Manset & P. Forshay, 451. https://arxiv.org/abs/1507.00034

Woo, J.-H., Bae, H.-J., Son, D., & Karouzos, M. 2016, ApJ, 817, 108, doi: 10.3847/0004-637X/817/2/108

Wright, E. L. 2006, PASP, 118, 1711, doi: 10.1086/510102

Wylezalek, D., Flores, A. M., Zakamska, N. L., Greene, J. E., & Riffel, R. A. 2020, MNRAS, 492, 4680, doi: 10.1093/mnras/staa062